SIAM J. IMAGING SCIENCES
Vol. 8, No. 1, pp. 403–425

Scale Invariant Metrics of Volumetric Datasets*

Dan Raviv† and Ramesh Raskar†

Abstract. Nature reveals itself in similar structures of different scales. A child and an adult share similar organs yet dramatically differ in size. Comparing the two is a challenging task to a computerized approach as scale and shape are coupled. Recently, it was shown that a local measure based on the Gaussian curvature can be used to normalize the local metric of a surface and then to extract global features and distances. In this paper we consider higher dimensions; specifically, we construct a scale invariant metric for volumetric domains which can be used in analysis of medical datasets such as computed tomography (CT) and magnetic resonance imaging (MRI).

Key words. scale invariant, differential geometry, Laplace–Beltrami, shape analysis

AMS subject classifications. 53B21, 58D17

DOI. 10.1137/140987675

1. Introduction.

A key idea in shape or image analysis is based on the design of invariants. Structures or images may look different on one regime, but given a different metric the true relationship is revealed. The study of metric invariants in computer vision was initiated more than 20 years ago in [8, 9], where geometry of planar curves under projective transformations was examined. Scale and affine transformations attracted the main focus [28], where global and local invariants [11] were used in the process. Other approaches, for example, based on scale-space signatures [10] and semidifferential invariants [24], were found useful and built the foundations for future schemes.

Images, on the other hand, require a different approach for designing invariants. Due to their high dimensionality, constructing invariants in images still remains a challenge in modern computer vision tasks. Lowe's milestone research on scale invariant feature transform (SIFT) [23] revolutionized the way we capture meaningful information in images. This was the beginning of an era where features became more sophisticated and were able to cleverly compensate for different deformations. Let us just mention SURF [2] and affine-SIFT (ASIFT) [25] as such predecessors. One more milestone we must mention was adopting the equi-affine metric into computer vision society [33], which was further used for important low-level vision tasks such as denoising.

Nonrigid shapes became popular in recent years modeling natural behavior. Faces, for example, can be considered as bendable shapes where different mimics still preserve the intrinsic (geodesic) distances between pairwise points [4]. While such distances can be evaluated in linear time [19, 38], their usage in comparison or alignment algorithms is not trivial. Shapes

*Received by the editors September 22, 2014; accepted for publication (in revised form) December 15, 2014; published electronically February 12, 2015.
http://www.siam.org/journals/siims/8-1/98767.html

†Media Lab, Massachusetts Institute of Technology (MIT), Cambridge, MA 02139 (darav@mit.edu, raskar@mit.edu).

were compared after their embedding into Euclidean domains [16], spherical spaces [15, 5], conformal disks or spheres [22], or even graphs [18, 37]. A direct embedding was also found useful and accurate [6] based on the minimization of the Gromov–Hausdorff distance. Trying to avoid unbounded distortions, a different approach was considered based on the embedding into the self-structure of the Riemannian geometry [3], which later was used to evaluate intrinsic distances and features [36, 26, 27, 7]. One of the useful tools that emerged from this research provided us with intrinsic distances, known as diffusion distances, based on the heat flow on the geometry [13]. Those average distances successfully replaced geodesic ones in some applications.

Measuring intrinsic distances or features depends on the method by which we evaluate the local metric. Traditionally, we consider a Riemannian metric to be locally Euclidean. Such an assumption provides an isometric invariant property, better known as a bending invariant. For many practical needs it is sufficient, as the stretching is minor, but the results rapidly degrade in quality when those assumptions do not hold. Trying to overcome such limitations for meaningful stretching, researchers have shown that a local metric for surfaces can be altered such that it compensates for scaling [1] by multiplying the metric with the magnitude of the Gaussian curvature; it can be equi-affine invariant [30] by considering a local volume preserving quadratic form, or it can even be fully affine invariant [31] by composition of a scale and equi-affine invariant metrics.

The need to model invariants in higher dimensions than two is clear. Computed tomography (CT) and magnetic resonance (MR) data of stretchable organs, such as the liver, the kidney, and the heart, are just a couple examples that can benefit from better alignment and learning algorithms. The geometry of those datasets suggests that one can do better than merely search for a continuous diffeomorphism. Recently, it was shown how to couple metric invariants into a nonrigid alignment algorithm and use it for tracking the left ventricle [32]; however, the alignment was done for textureless surfaces and did not take into account all the information that appears in the data.

We need to develop a new theory compensating for local stretching in shapes of dimensions greater than two. Moving toward volumetric data is not straightforward, as manipulating the metric in two dimensions (surfaces) was based on the Gaussian curvature, which is not even defined for volumes. In this work we begin by examining scale invariant signatures in curves from a level-set approach. We reexamine scale invariant metrics of surfaces, and we begin the journey of designing differential invariants in volumetric datasets.

The paper is organized as follows: We present a short description of the notation in section 2, followed by section 3, where we provide a brief summary of spectral geometry. Sections 4 and 5 provide a short summary on scale invariants of curves and surfaces, including a fresh look through level sets. Section 6 is dedicated to scale invariants in volumetric data. We explore two different scenarios, with and without photometric change, and provide the mathematical construction and proof of invariance for both. In section 7 we numerically validate the results in various examples.

2. Definitions. The majority of this paper requires basic knowledge of differential geometry. Specifically, we model a curve as a continuous regular function $C(t)$ such that

$$\begin{aligned} &C : [0,1] \to \mathbb{R}^2, \\ &C(t) = (x(t), y(t)), \end{aligned} \tag{2.1}$$

and its derivative $\frac{\partial C}{\partial t}$ is well defined for all t. We further consider a surface S as a compact two-dimensional (2D) Riemannian manifold with a metric tensor g, where

$$\begin{aligned} &S : U \subset \mathbb{R}^2 \to \mathbb{R}^3, \\ &g_{ij} = \langle S_i, S_j \rangle, \end{aligned} \tag{2.2}$$

using the shorthand notation $S_1 = \partial S/\partial u$, $S_2 = \partial S/\partial v$, where u and v are the coordinates of U. An infinitesimal displacement ds on the surface is thereby given by

$$ds^2 = g_{11}du^2 + 2g_{12}dudv + g_{22}dv^2. \tag{2.3}$$

The metric coefficients (g_{ij}) transform the surface's parametrization coordinates u and v into a Euclidean distance measure.

Considering images as manifolds was shown to be a successful approach [20] and can be used for higher dimensions as well. Specifically, volumetric datasets, such as those constructed from CT or MR imaging (MRI), can be regarded as compact three-dimensional (3D) Riemannian manifolds, again with a metric tensor g, now given by a symmetric semi-positive definite 3×3 matrix. Its six coefficients represent a local distance in the measured space. We can define a volumetric Riemannian manifold as a graph V,

$$\begin{aligned} &V : \mathbb{R}^3 \to \mathbb{R}^4, \\ &V(u,v,w) = (u,v,w,I(u,v,w)), \end{aligned} \tag{2.4}$$

where $I(u,v,w) \in \mathbb{R}$ is a scalar value representing the local intensity.

Useful notations in this work, well studied in differential geometry, are the Christoffel symbols of the first or second kind. Such coefficients provide a coordinate expression for the Levi-Civita connection and are used to express the Riemannian curvature tensor. Given a local coordinate system $\frac{\partial}{\partial x^i}$, where $x^1 = u$, $x^2 = v$, and $x^3 = w$ in our setup, the coefficients of the second kind can be defined directly from the metric and its derivatives;

$$\Gamma_{cab} = \frac{1}{2}\left(\frac{\partial g_{ca}}{\partial x^b} + \frac{\partial g_{cb}}{\partial x^a} + \frac{\partial g_{ab}}{\partial x^c}\right), \tag{2.5}$$

and the symbols of the first kind are given by

$$\Gamma_{cab} = g_{cd}\Gamma^d_{ab}, \tag{2.6}$$

where Einstein's summation notation is used.

3. Spectral geometry: Think globally; act locally. In this paper we construct distances and features on the manifolds generated from the proposed metrics using the spectral geometry framework. We will encounter the terms summarized here only in the numerical validation section.

Spectral geometry, also referred to as diffusion geometry, introduced in [13, 12], deals with geometric analysis of metric spaces where geodesic distances are replaced by integral difference between heat kernels. Conceptually, this formulation allows us to think of a global distance while evaluating a local metric.

The starting point of this approach relies on the *heat equation*

$$\left(\frac{\partial}{\partial t} + \Delta_h\right) f(x,t) = 0, \tag{3.1}$$

which describes the propagation of heat, where $f(x,t)$ is the heat distribution at a point x in time t. Initial conditions are given by $f(x,0)$, and Δ_h is the Laplace–Beltrami operator with respect to the metric h. The fundamental solution of (3.1) is called a *heat kernel*, and using spectral decomposition it can be written as

$$k_t(x,x') = \sum_{i\geq 0} e^{-\lambda_i t}\phi_i(x)\phi_i(x'), \tag{3.2}$$

where ϕ_i and λ_i are the corresponding eigenfunctions and eigenvalues of the Laplace–Beltrami operator satisfying

$$\Delta_h \phi_i = \lambda_i \phi_i. \tag{3.3}$$

The value of the heat kernel $k_t(x,x')$ can be interpreted as the transition probability density of a random walk of length t from point x to point x'. The length or time t defines a family of diffusion distances

$$\begin{aligned} d_t^2(x,x') &= \int \big(k_t(x,\cdot) - k_t(x',\cdot)\big)^2\, da \\ &= \sum_{i>0} e^{-2\lambda_i t}(\phi_i(x) - \phi_i(x'))^2 \end{aligned} \tag{3.4}$$

between any two points x and x'. The parameter t can be given the meaning of *scale*, and the family $\{d_t\}$ can be thought of as the scale-space of metrics. Integrating over t can be interpreted as the connectivity rate by paths of any length (time) and is referred to as the *commute-time distance* [29]. Specifically,

$$\begin{aligned} d_{\mathrm{CT}}^2(x,x') &= \int_0^\infty d_t^2(x,x')dt \\ &= \sum_{i>0} \frac{1}{2\lambda_i}(\phi_i(x) - \phi_i(x'))^2. \end{aligned} \tag{3.5}$$

4. Scale invariant length of curves. We begin this exploration of invariants in a simple scenario of curves in $\mathbb{R}^2$. Consider a curve $C(t) = (x(t), y(t))$ in the domain $t \in [0, 1]$. The length of the curve L is given by

$$L = \int_0^1 \sqrt{\dot{x}^2 + \dot{y}^2} dt, \tag{4.1}$$

while the length of the scaled curve $\tilde{C} = \alpha C$ becomes

$$\tilde{L} = \int_0^1 \sqrt{\alpha^2 \dot{x}^2 + \alpha^2 \dot{y}^2} dt = \alpha L, \tag{4.2}$$

since $\frac{\partial \alpha x}{\partial t} = \alpha \frac{\partial x}{\partial t}$. Note that throughout the paper we use the $\tilde{Y}$ notation for indicating a scaled quantity Y by an unknown factor α.

Even if we do not know a priori what α is, we can normalize the length of the curve using the second derivative in such a way that scaling will not alter the metric. The new length measurement will be different from the original one, and we will lose some information about the shape, but it will be invariant to scaling. This is a fundamental concept that will follow us throughout this paper for all dimensions. Specifically, we consider the curve's curvature κ,

$$\kappa(t) = \frac{|\dot{x}\ddot{y} - \dot{y}\ddot{x}|}{(\dot{x}^2 + \dot{y}^2)^{\frac{3}{2}}}, \tag{4.3}$$

and its scaled version,

$$\tilde{\kappa}(t) = \frac{\alpha^2}{\alpha^3}\kappa = \frac{1}{\alpha}\kappa. \tag{4.4}$$

Corollary 4.1. *κdL is a scale invariant differential length measurement.*

Proof. From (4.2) and (4.4) it follows that $\tilde{\kappa} d\tilde{L} = \kappa dL$, which means that κdL is scale invariant. ∎

Notice that once the curvature vanishes (e.g., $\kappa = 0$), the metric is not defined. One cannot use curvature to normalize for scale if there is no meaningful structure from which to infer. We will refer to this metric as a *pseudometric* due to this observation.

Let us re-examine the local invariant metric using a level-set approach. A curve can be written as the zero (or any other constant) level set of an implicit function $F(x, y)$ (specifically $F(x, y) = 0$), and consequently

$$\nabla F = \left(\frac{\partial F}{\partial x}, \frac{\partial F}{\partial y}\right)^T = (F_x, F_y)^T,$$
$$H(F) = \begin{pmatrix} F_{xx} & F_{xy} \\ F_{yx} & F_{yy} \end{pmatrix}. \tag{4.5}$$

Since the gradient of F is perpendicular to the tangent of its level-set curves $F(x, y) = c$, it must be parallel to the normal along the level sets. This leads to the known mean curvature formula [35, 17]

$$\kappa = \frac{\bar{\nabla} F^T H(F) \bar{\nabla} F}{||\nabla F||^3}, \tag{4.6}$$

where $\bar{\nabla}F = (-F_y, F_x)^T$.

Denoting $\tilde{x} = \alpha x$ and $\tilde{y} = \alpha y$, we consider the scaled level set $\tilde{F}$:

$$\tilde{F} = F(\tilde{x}, \tilde{y}) = F(\alpha x, \alpha y). \tag{4.7}$$

Since $\frac{\partial \tilde{F}}{\partial \tilde{x}} = \frac{\partial F}{\partial x}\frac{\partial x}{\partial \tilde{x}} = \frac{1}{\alpha}\frac{\partial F}{\partial x}$, we realize that

$$\begin{aligned} \nabla\tilde{F} &= \left(\tilde{F}_{\tilde{x}}, \tilde{F}_{\tilde{y}}\right)^T = \alpha^{-1}\left(F_x, F_y\right)^T = \alpha^{-1}\nabla F^T, \\ H(\tilde{F}) &= \begin{pmatrix} \tilde{F}_{\tilde{x}\tilde{x}} & \tilde{F}_{\tilde{x}\tilde{y}} \\ \tilde{F}_{\tilde{y}\tilde{x}} & \tilde{F}_{\tilde{y}\tilde{y}} \end{pmatrix} = \alpha^{-2}H(F). \end{aligned} \tag{4.8}$$

We conclude that the curvature of the scaled level set is $\frac{1}{\alpha}$ that of the original one. Specifically, we have the following.

Corollary 4.2. $\tilde{\kappa} = \frac{\bar{\nabla}\tilde{F}^T H(\tilde{F})\bar{\nabla}\tilde{F}}{||\nabla\tilde{F}||^3} = \frac{1}{\alpha}\kappa$.

Proof. From (4.8) we realize that

$$\tilde{\kappa} = \frac{\alpha^{-1}\alpha^{-2}\alpha^{-1}}{((\alpha^{-2})^{0.5})^3}\kappa = \frac{\alpha^{-4}}{\alpha^{-3}}\kappa = \alpha^{-1}\kappa. \tag{4.9}$$ ■

Theorem 4.3. *κds is a scale invariant differential level-set measurement.*

Proof. From Corollary 4.2 we infer that

$$\tilde{\kappa}d\tilde{s} = \frac{1}{\alpha}\kappa\alpha ds = \kappa ds, \tag{4.10}$$

which concludes the proof. ■

5. Scale invariant metric for surfaces. A scale invariant metric for surfaces was first introduced in [1], where the authors showed that multiplying the coefficients of the first fundamental form by the Gaussian curvature produces a scale invariant metric. We summarize their result in this section.

The Gaussian curvature K_G can be defined by the ratio between the determinant of the second and first fundamental forms,

$$K_G = \frac{\det b}{\det g} = \frac{b_{11}b_{22} - b_{12}^2}{g_{11}g_{22} - g_{12}^2}, \tag{5.1}$$

where $b_{ij} = \langle S_{ij}, n\rangle$ and $n = \frac{S_1 \times S_2}{||S_1 \times S_2||}$.

An α scaling of the surface S expands the coefficients of the first fundamental form by α^2 as

$$\tilde{g}_{ij} = \langle \alpha S_i, \alpha S_j\rangle = \alpha^2\langle S_i, S_j\rangle = \alpha^2 g_{ij} \tag{5.2}$$

and alters the coefficients of the second fundamental form by α since

$$\tilde{b}_{ij} = \langle \alpha S_{ij}, n\rangle = \alpha\langle S_{ij}, n\rangle = \alpha b_{ij}. \tag{5.3}$$

Corollary 5.1. *$|K_G|g_{ij}$ is a scale invariant metric for surfaces* [1].

Proof. We plug (5.2) and (5.3) into the Gaussian curvature of the scaled surface $\tilde{K}_G$,

$$|\tilde{K}_G|\tilde{g}_{ij} = \left|\frac{\det \tilde{b}}{\det \tilde{g}}\right| \tilde{g}_{ij} = \frac{\alpha^2}{\alpha^4}|K_G|\alpha^2 g_{ij} = |K_G|g_{ij}, \tag{5.4}$$

and conclude that $|K_G|g_{ij}$ is a scale invariant metric. ∎

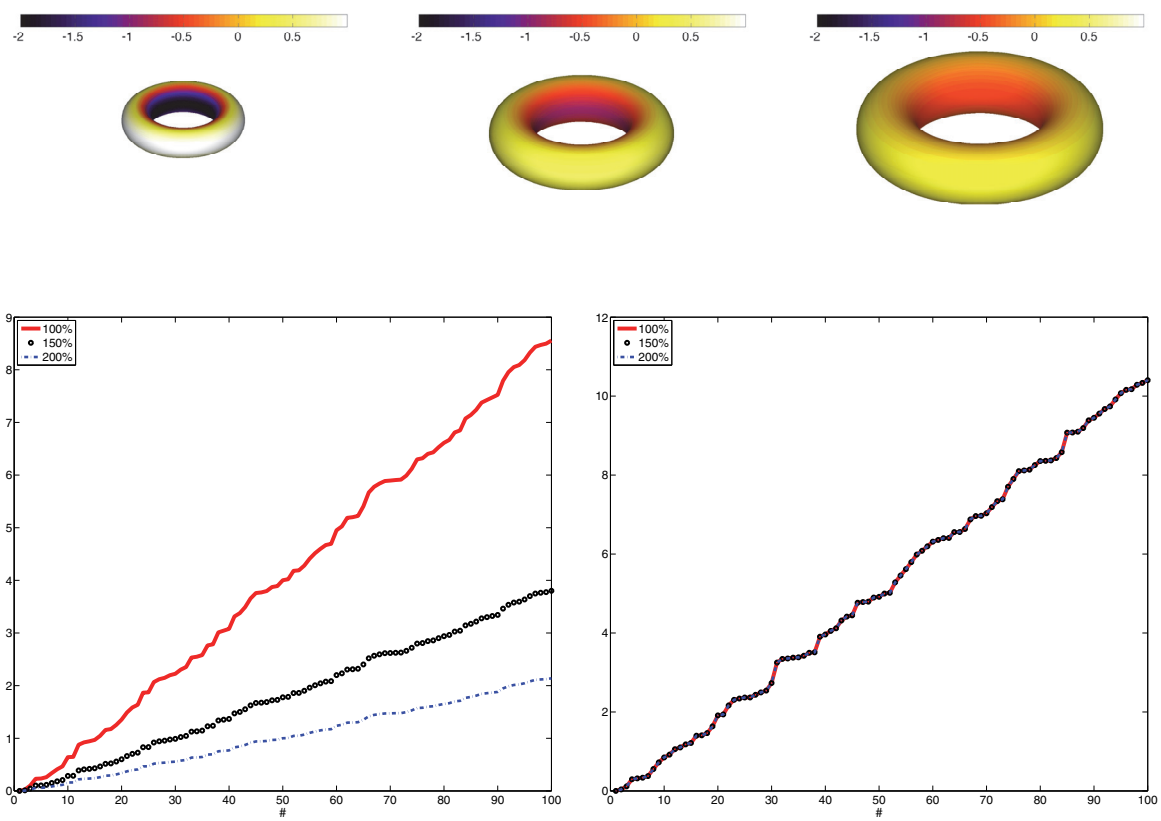

Figure 1. *Eigenvalues of the Laplace–Beltrami operator of a scaled torus ($\times 1$, $\times 1.5$, and $\times 2$). In the top row we depict the three versions of the shape overlaid with its scalar curvature. At the bottom left, we show the first (smallest)* 100 *eigenvalues of the Laplace–Beltrami operator using a Euclidean metric, and on the bottom right we use the scale invariant metric.*

6. Scale invariant metrics for volumetric data.

6.1. Scaling of what? Moving forward from surfaces to volumes introduces a new metric on the data—usually a coupled measure between geometry and photometry [20, 21]. Specifically, we define the volumetric manifold $V : \mathbb{R}^3 \to \mathbb{R}^4$ to be a graph on the spatial coordinates, as $V(x, y, z) = (x, y, z, I(x, y, z))$. The local metric g_{ij} is a 3×3 semi-positive definite matrix (six coefficients), which can be written as

$$G = (g_{ij}) = \begin{pmatrix} 1 + I_x^2 & I_x I_y & I_x I_z \\ I_x I_y & 1 + I_y^2 & I_y I_z \\ I_x I_z & I_y I_z & 1 + I_z^2 \end{pmatrix}. \tag{6.1}$$

Notice that the local length measurement ds becomes

$$\begin{aligned} ds^2 &= dx^2 + dy^2 + dz^2 + dI^2 \\ &= dx^2 + dy^2 + dz^2 + (I_x dx + I_y dy + I_z dz)^2 \\ &= (1 + I_x^2)dx^2 + (1 + I_y^2)dy^2 + (1 + I_z^2)dz^2 \\ &\quad + 2I_x I_y dxdy + 2I_x I_z dxdz + 2I_y I_z dydz \\ &= [dx, dy, dz]G[dx, dy, dz]^T. \end{aligned} \tag{6.2}$$

A fundamental question we must address, as the name of this subsection states, is *scaling of what?* We can think of three options:

- Geometric and photometric together, which is a uniform scaling of the manifold's metric.
- Photometric alone: The structure is unchanged, but the intensity is altered. An example is MRI data in which a tumor starts to appear and the change in local density becomes visible.
- Geometric alone: The structure is scaled while preserving its intensity. An example is a CT image of a stretchable organ.

Generating a scale invariant metric on a 3D manifold (first option) is interesting by itself but may not have an immediate application, as the intensity and spatial coordinates are scaled by the same factor. We will derive this formulation in the next section, as it answers a fundamental question in geometry. In this scenario we will consider the scalar curvature instead of the Gaussian curvature in the construction of an invariant metric. We then restrict ourselves to the photometric metric alone (second option). While it is tempting to normalize only the photometric part of the metric, we will show that it cannot be achieved in the proposed approach. Finally, we consider a change in structure alone (third option). We wish to limit ourselves to stretches of the geometry within the volume, without any change of the photometry. We will solve this problem by introducing a level-set–based invariant metric.

6.2. Scale invariant metric of a 3D manifold. For surfaces (2D manifolds) we normalized the metric using the Gaussian curvature. For 3D data we propose using the trace of the Ricci curvature, also known as the scalar curvature. Geometrically it relates to the amount by which the volume of a geodesic ball deviates with relation to a Euclidean one. In two dimensions, the scalar curvature is exactly twice that of the Gaussian curvature, which means that it can also be used for surface normalization.

The Ricci curvature tensor is well studied in the literature, and here we provide a short useful summary. Please refer to [14, 35] for further details. The $[1,3]$ curvature tensor R^l_{ijk} can be explicitly written from the Christoffel symbols of the second kind,

$$R^l_{ijk} = \frac{\partial}{\partial i}\Gamma^l_{jk} + \Gamma^m_{ik}\Gamma^l_{jm} - \frac{\partial}{\partial j}\Gamma^l_{ik} - \Gamma^m_{jk}\Gamma^l_{im}, \tag{6.3}$$

from which we define the $[0,4]$ curvature tensor R_{ijkl},

$$R_{ijkl} = R^m_{ijk} g_{lm}, \tag{6.4}$$

and the $[0,2]$ curvature R_{ij},

$$R_{ij} = g^{kl} R_{kijl}. \tag{6.5}$$

The scalar curvature Sc is the trace of R_{ij} and is defined by

$$Sc = g^{ij} R_{ij}. \tag{6.6}$$

Let us consider an α scaling of the manifold V into $\tilde{V}$; then, the coefficients of the inverse metric g^{ij} will scale by α^{-2}, and the Christoffel symbols of the second kind will not change, as shown in the following two corollaries.

Corollary 6.1. *An α scaling of the manifold V will alter the coefficients of the inverse metric by α^{-2}.*

Proof. Since $g_{ij}g^{ij} = identity$ and $\tilde{g}_{ij} = \alpha^2 g_{ij}$, it immediately follows that $\tilde{g}_{ij}\frac{1}{\alpha^2}g^{ij} = identity$, from which we conclude that $\tilde{g}^{ij} = \frac{1}{\alpha^2}g^{ij}$. ∎

Corollary 6.2. *An α scaling of the manifold V will not change the Christoffel symbols of the second kind.*

Proof. From Corollary 6.1 and definitions (2.5) and (2.6),

$$\begin{aligned}
\tilde{\Gamma}^k_{ij} &= \frac{1}{2}\tilde{g}^{km}\left(\frac{\partial \tilde{g}_{jm}}{\partial i} + \frac{\partial \tilde{g}_{im}}{\partial j} + \frac{\partial \tilde{g}_{ij}}{\partial m}\right) \\
&= \frac{1}{2\alpha^2}g^{km}\left(\alpha^2\frac{\partial g_{jm}}{\partial i} + \alpha^2\frac{\partial g_{im}}{\partial j} + \alpha^2\frac{\partial g_{ij}}{\partial m}\right) \\
&= \frac{1}{2}g^{km}\left(\frac{\partial g_{jm}}{\partial i} + \frac{\partial g_{im}}{\partial j} + \frac{\partial g_{ij}}{\partial m}\right) = \Gamma^k_{ij}.
\end{aligned} \tag{6.7}$$

∎

It follows that multiplying the local metric by the size of the scalar curvature is a volumetric invariant metric.

Theorem 6.3. *$|Sc|g_{ij}$ is a scale invariant volumetric metric.*

Proof. From Corollaries 6.1 and 6.2 and definitions (6.3), (6.4), (6.5), and (6.6) we readily have

$$\begin{aligned}
\tilde{R}^l_{ijk} &= R^l_{ijk}, \\
\tilde{R}_{ijkl} &= \tilde{R}^m_{ijk}\tilde{g}_{lm} = R^m_{ijk}g_{lm}\alpha^2, \\
\tilde{R}_{ij} &= \tilde{g}^{kl}R_{kijl} = \frac{1}{\alpha^2}g^{kl}R_{ijkl}\alpha^2 = R_{ij}, \\
\tilde{Sc} &= \tilde{g}^{ij}\tilde{R}_{ij} = \frac{1}{\alpha^2}g^{ij}R_{ij} = \frac{1}{\alpha^2}Sc.
\end{aligned} \tag{6.8}$$

Since $\tilde{g}_{ij} = \alpha^2 g_{ij}$, we infer that

$$|\tilde{Sc}|\tilde{g}_{ij} = \left|\frac{1}{\alpha^2} Sc\right| \alpha^2 g_{ij} = |Sc| g_{ij}, \tag{6.9}$$

which concludes the proof. ∎

Note that we did not use the fact that the manifold is of dimension three; hence, it is true for any dimension. We summarize that the scalar curvature can be used to normalize the metric of a Riemannian manifold into its scale invariant form.

Can we use the normalization scheme presented above to build a metric that is scale invariant only to the photometric part? It is tempting to try to normalize the photometric part out of its curvature, but, as we will shortly see, it is not possible.

Let us revisit the length measurement derived from (6.1). We wish that only the intensity would be invariant to scaling, meaning $dx = d\tilde{x}$, $dy = d\tilde{y}$, and $dz = d\tilde{z}$. Hence, the length measurement $\tilde{ds}$ becomes

$$\begin{aligned} d\tilde{s}^2 &= dx^2 + dy^2 + dz^2 + d\tilde{I}^2 \\ &= dx^2 + dy^2 + dz^2 + (\tilde{I}_x d_x + \tilde{I}_y d_y + \tilde{I}_z dz)^2. \end{aligned} \tag{6.10}$$

We can also think of G as the sum of the geometric and photometric parts

$$G = (g_{ij}) = \begin{pmatrix} 1 & 0 & 0 \\ 0 & 1 & 0 \\ 0 & 0 & 1 \end{pmatrix} + \begin{pmatrix} I_x^2 & I_x I_y & I_x I_z \\ I_x I_y & I_y^2 & I_y I_z \\ I_x I_z & I_y I_z & I_z^2 \end{pmatrix} = \mathcal{I}_{3\times 3} + P, \tag{6.11}$$

where $\mathcal{I}_{3\times 3}$ is the identity matrix and $P = (P_{ij})$ is the photometric part. It is extremely tempting to normalize P according to its curvature and generate a photometric scale invariant metric. Unfortunately, as the next corollary shows, it cannot be done.

Corollary 6.4. *The photometric part $P = G - \mathcal{I}_{3\times 3}$ of a graph has a degenerate determinant.*

Proof. Let us rewrite P as the multiplication of two matrices P_A and P_B:

$$\begin{aligned} P &= \begin{pmatrix} I_x^2 & I_x I_y & I_x I_z \\ I_x I_y & I_y^2 & I_y I_z \\ I_x I_z & I_y I_z & I_z^2 \end{pmatrix} \\ &= \begin{pmatrix} I_x & 0 & 0 \\ 0 & I_y & 0 \\ 0 & 0 & l_z \end{pmatrix} \begin{pmatrix} I_x & I_y & I_z \\ I_x & I_y & I_z \\ I_x & I_y & I_z \end{pmatrix} = P_A P_B. \end{aligned} \tag{6.12}$$

Since $\det(P) = \det(P_A)\det(P_B)$ and $\det(P_B)$ is zero, we conclude that P always has a degenerate determinant. ∎

6.3. Geometric invariant metric: Level-set approach. Constructing a scale invariant metric for volumes following the footsteps of the successful 2D scale invariant metric [1] is problematic. As seen earlier, it is doable using the scalar curvature, but in practice it is not the scaling invariant we expect from data captured out of tomography machinery such as

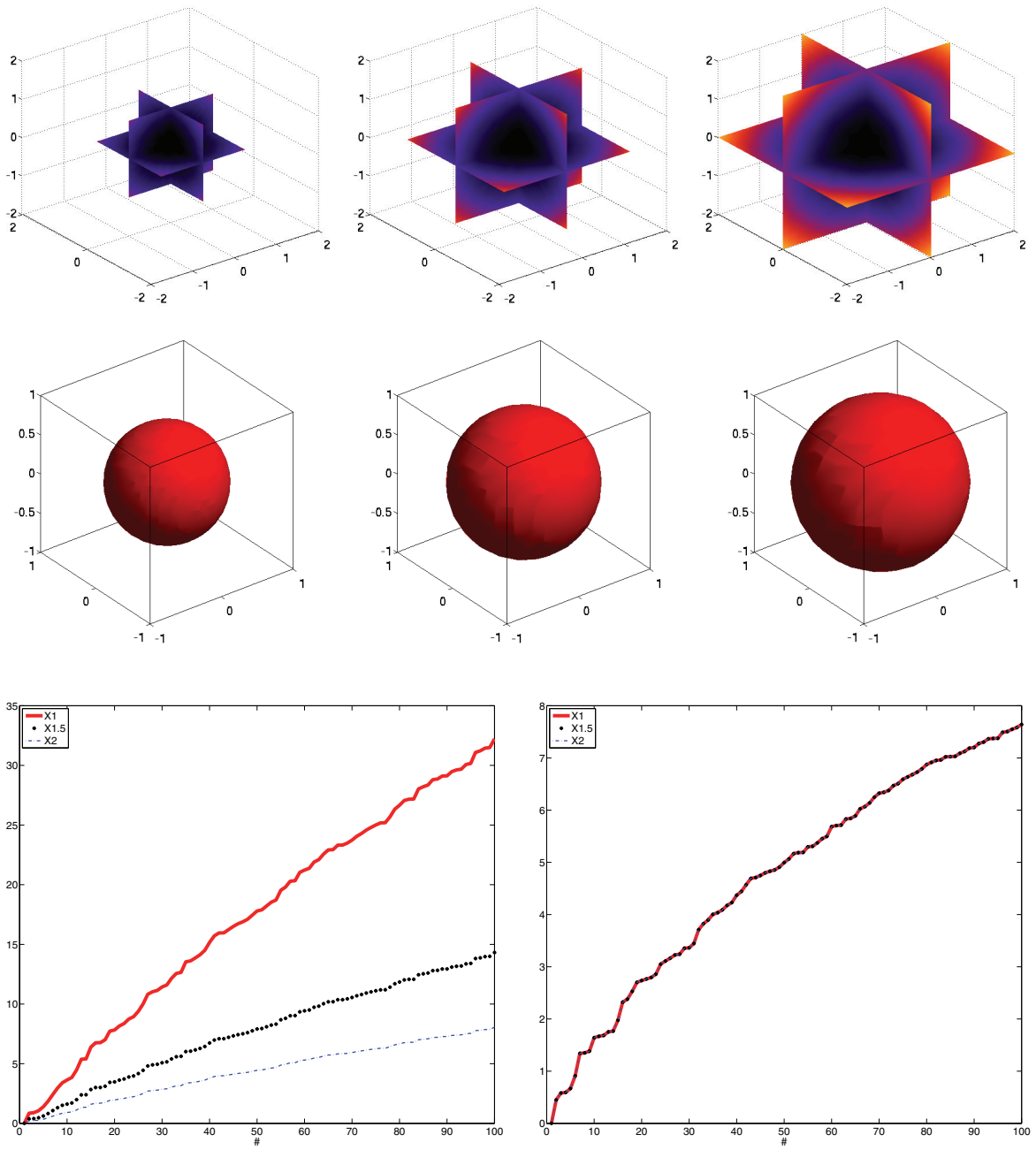

Figure 2. *Eigenvalues of the Laplace–Beltrami operator of scaled 3-spheres (×1, ×1.5, and ×2). Notice that it is a volumetric sphere and not a surface, where the color represents the third dimension. We depict slices (top row) of three versions of the shape overlaid with their scalar curvature, and one similar level set (middle row) for all three shapes. Using the Euclidean metric (bottom left), we see that the eigenvalues of the Laplace–Beltrami operator alter dramatically, while using the scale invariant metric (bottom right), we get an almost perfect invariance.*

CT and MR. We cannot consider the curvature of the manifold for normalization since the intensity is not scaled. In addition, we cannot ignore the intensities because without them shortest paths are straight lines, which means no curvature exists.

We need to rethink the invariance in such datasets, and one potential solution is to construct invariant metrics based on the level sets of the data. The intensities along level sets do not change by definition, yet the geometry they construct should remain invariant—meaning that the curvature in question is the Gaussian curvature of the 2D level set of the volumetric domain.

Let $F(x, y, z) = 0$ be an implicit surface, and define its gradient ∇F and Hessian $H(F)$ as follows:

$$\nabla F = \left(\frac{\partial F}{\partial x}, \frac{\partial F}{\partial y}, \frac{\partial F}{\partial z}\right)^T = (F_x, F_y, F_z)^T,$$
$$H(F) = \begin{pmatrix} F_{xx} & F_{xy} & F_{xz} \\ F_{yx} & F_{yy} & F_{yz} \\ F_{xz} & F_{yz} & F_{zz} \end{pmatrix}. \tag{6.13}$$

It can be shown that the Gaussian curvature is a function of ∇F and H.

Corollary 6.5.

$$K_g = -\frac{\det \begin{bmatrix} H(F) & \nabla F \\ \nabla F^T & 0 \end{bmatrix}}{|\nabla F|^2}. \tag{6.14}$$

Proof. See [35, 17]. ∎

Denoting $\tilde{F} = \tilde{F}(\tilde{x}, \tilde{y}, \tilde{z}) = F(\alpha x, \alpha y, \alpha z)$ as the scaled level set function, and realizing that $\frac{\partial \tilde{F}}{\partial \tilde{x}} = \alpha^{-1} \frac{\partial F}{\partial x}$, and similarly for y and z, we infer that

$$\nabla \tilde{F} = \left(\tilde{F}_{\tilde{x}}, \tilde{F}_{\tilde{y}}, \tilde{F}_{\tilde{z}}\right)^T = \frac{1}{\alpha} (F_x, F_y, F_z)^T = \alpha^{-1} \nabla F^T,$$
$$H(\tilde{F}) = \begin{pmatrix} \tilde{F}_{\tilde{x}\tilde{x}} & \tilde{F}_{\tilde{x}\tilde{y}} & \tilde{F}_{\tilde{x}\tilde{z}} \\ \tilde{F}_{\tilde{y}\tilde{x}} & \tilde{F}_{\tilde{y}\tilde{y}} & \tilde{F}_{\tilde{y}\tilde{z}} \\ \tilde{F}_{\tilde{x}\tilde{z}} & \tilde{F}_{\tilde{y}\tilde{z}} & \tilde{F}_{\tilde{z}\tilde{z}} \end{pmatrix} = \frac{1}{\alpha^2} H(F). \tag{6.15}$$

We conclude that the curvature of the scaled level set is $\frac{1}{\alpha^2}$ that of the original one. Specifically, we have the following corollary.

Corollary 6.6. $\tilde{K}_g = \frac{1}{\alpha^2} K_g$.

Proof. We can rewrite the Gaussian curvature K_g as (see [17])

$$K_g = \frac{\nabla F^T H^*(F) \nabla F}{|\nabla F|^4}, \tag{6.16}$$

where

$$H^*(F) = \begin{bmatrix} F_{yy}F_{zz} - F_{yz}F_{zy}, & F_{yz}F_{zx} - F_{yx}F_{zz}, & F_{yx}F_{zy} - F_{yy}F_{zx} \\ F_{xz}F_{zy} - F_{xy}F_{zz}, & F_{xx}F_{zz} - F_{xz}F_{zx}, & F_{xy}F_{zx} - F_{xx}F_{zy} \\ F_{xy}F_{yz} - F_{xz}F_{yy}, & F_{yx}F_{xz} - F_{xx}F_{yz}, & F_{xx}F_{yy} - F_{xy}F_{yx} \end{bmatrix}.$$

From (6.14), (6.15), and (6.16) we readily have

$$\begin{aligned}\tilde{K}_g &= \frac{\nabla\tilde{F}^T H^*(\tilde{F})\nabla\tilde{F}}{|\nabla\tilde{F}|^4} \\ &= \frac{\alpha^{-1}\nabla F^T \alpha^{-4} H^*(F)\alpha^{-1}\nabla F}{\alpha^{-4}|\nabla F|^4} = \frac{1}{\alpha^2}K_g. \end{aligned} \tag{6.17}$$

■

Theorem 6.7. *$|K_g|\mathcal{I}_{3\times3}$ is a level-set scale invariant metric of volumetric data.*

Proof. We notice that by definition P (the photometric part of the metric) does not change along a level set, meaning the photometric part of the metric vanishes (e.g., $dI = 0$ on the level set). Hence, after α scaling it still has no contribution.

Since $\tilde{\mathcal{I}}_{3\times3} = \alpha^2\mathcal{I}_{3\times3}$ (e.g., the geometry grid is scaled), and given Corollary 6.6, we infer that along a fixed level set

$$|\tilde{K}_g|\tilde{\mathcal{I}}_{3\times3} = \frac{1}{\alpha^2}|K_g|\alpha^2\mathcal{I}_{3\times3} = |K_g|\mathcal{I}_{3\times3}. \tag{6.18}$$

■

It is interesting to notice that this metric does not rely on the values of the intensities but only on the level sets they generate. Notice that in positions where the curvature vanishes the metric is not defined. Those are the locations where the intensity does not change in one or more directions. While we can simply ignore those places by squeezing them into an ϵ-sized volume, a better strategy will be to interpolate the curvature. That is, we consider positions with curvature above some threshold to be valid and interpolate for the rest of the domain. This approach is reasonable if we believe that meaningful curvatures are indicators of local stretches which are not visible in all places.

An additional result regarding images can be inferred from Theorem 6.7. We can rewrite the same metric for images, compensating for 2D stretching. The derivatives of the structure are restricted to I_x and I_y, and the identity is a 2×2 matrix.

7. Numerical validation.

We explored a change in scaling for a horizontal slice (an image) and a volumetric dataset. The data used for this validation is the brain atlas MNI152 T1 1mm taken from the FSL open database [34]. We explored curvature change, eigendecomposition of the Laplace–Beltrami operator, heat kernel signatures (HKS), and commute time distances. Comparisons were performed with relation to the ground truth of the deformations.

In order to evaluate the local metrics, Christoffel symbols, and the different curvature tensors, we used a finite difference numerical scheme. As the derivations along the principle directions are orthogonal and parallel to the grid, their calculation is trivial. A well-known formulation of the Laplace–Beltrami operator in local coordinates $\mathbf{u} = (u_1, u_2, u_3)^{\mathrm{T}}$ is

$$\Delta f = \frac{1}{\sqrt{\det \mathbf{G}}}\frac{\partial^{\mathrm{T}}}{\partial \mathbf{u}}\left(\sqrt{\det \mathbf{G}}\mathbf{G}^{-1}\frac{\partial}{\partial \mathbf{u}}f\right), \tag{7.1}$$

where the sign is flipped to impose a semipositive structure, $\frac{\partial}{\partial \mathbf{u}} = (\frac{\partial}{\partial u_1}, \frac{\partial}{\partial u_2}, \frac{\partial}{\partial u_3})^{\mathrm{T}}$ and $\mathbf{G} = (g_{ij}) \in \mathbb{R}^{3\times3}$. Moving from the continuous definition toward a numerical scheme, we generated forward and backward derivative matrices for the three main axes x, y, and z, denoted by D_1^+, D_1^-, D_2^+, D_2^-, and D_3^+, D_3^-, respectively. We further generated a diagonal matrix composed

of the square root of the metric's determinant and its inverse, denoted by M and M^{-1}, and the diagonal matrices G^{ij}, where g^{ij} for each point appears on the diagonal. It follows that the Laplace–Beltrami operator L can be written as a matrix by

$$L = \sum_{i=1}^{3} \sum_{j=1}^{3} M^{-1} D_i^- M G^{ij} D_j^+. \tag{7.2}$$

We used MATLAB 2014a for its eigendecomposition. We first examine two toy examples of a scaled torus (Figure 1) and a scaled 3-sphere (Figure 2), where we normalize the metric according to scalar curvature, and generate a scale invariant Laplace–Beltrami operator.

The curvature in many locations is significant enough to construct a scale invariant metric, both for 2D slices and the 3D volume. Notice that the curvatures along the image's level sets are scaled by the inverse magnitude of the deformation, while the curvatures of the volume's level sets are scaled by the inverse squared magnitude. In the graphs that follow, we square rooted the second.

In Figure 3 we visualize the significant curvatures measured in one 2D slice. We cannot collect meaningful data in all positions, as flat regions have vanishing curvatures, and in practice near-flat regions appear unstable for curvature estimation. The global scale factor is calculated as the median for all measurements and is locally visualized on the slice using a moving median window ($10\% \times 10\%$). We experimented with different thresholds of the curvature and found this parameter to be stable. In addition, we chose inliers as points with up to three standard deviations. The results are summarized in the graphs shown in Figure 4. We explored different thresholds from 10^{-5} to 5×10^{-2} of the magnitude of the measured curvature deciding whether a point should be considered an inlier. The results showed robustness to this feature. We did notice a slight reduction in accuracy of 3%–4% around the scaling factor of 1.4. This is not that surprising as the scaling is done on subpixel values. Yet we were amazed by the achieved accuracy.

Next, we explored the level-set curvatures of the entire volumetric brain. Once again, we were able to get a stable reading of the curvature in many locations to infer the scaling. The curvature was altered by one over the scaling factor squared. In Figure 5 we depict the results, and in Figure 6 we show stability graphs for different thresholds of the curvature. In this scenario we also chose outliers according to large shifts from the standard deviation. Notice that we provide the ratio between the curvatures where the true alignment is known a priori.

Scaling the local metric can compensate for changes in spectral signatures. We computed the eigenvalues and eigenvectors of the Laplace–Beltrami operator on two differently scaled images. From this decomposition we further approximated HKS in a wide range of temporal sampling. In Figure 7 we depict the two images, the magnitude of their local curvatures, and the relevant histograms to assist in visualizing the differences. We further depict in a log-log graph HKS for matching points.

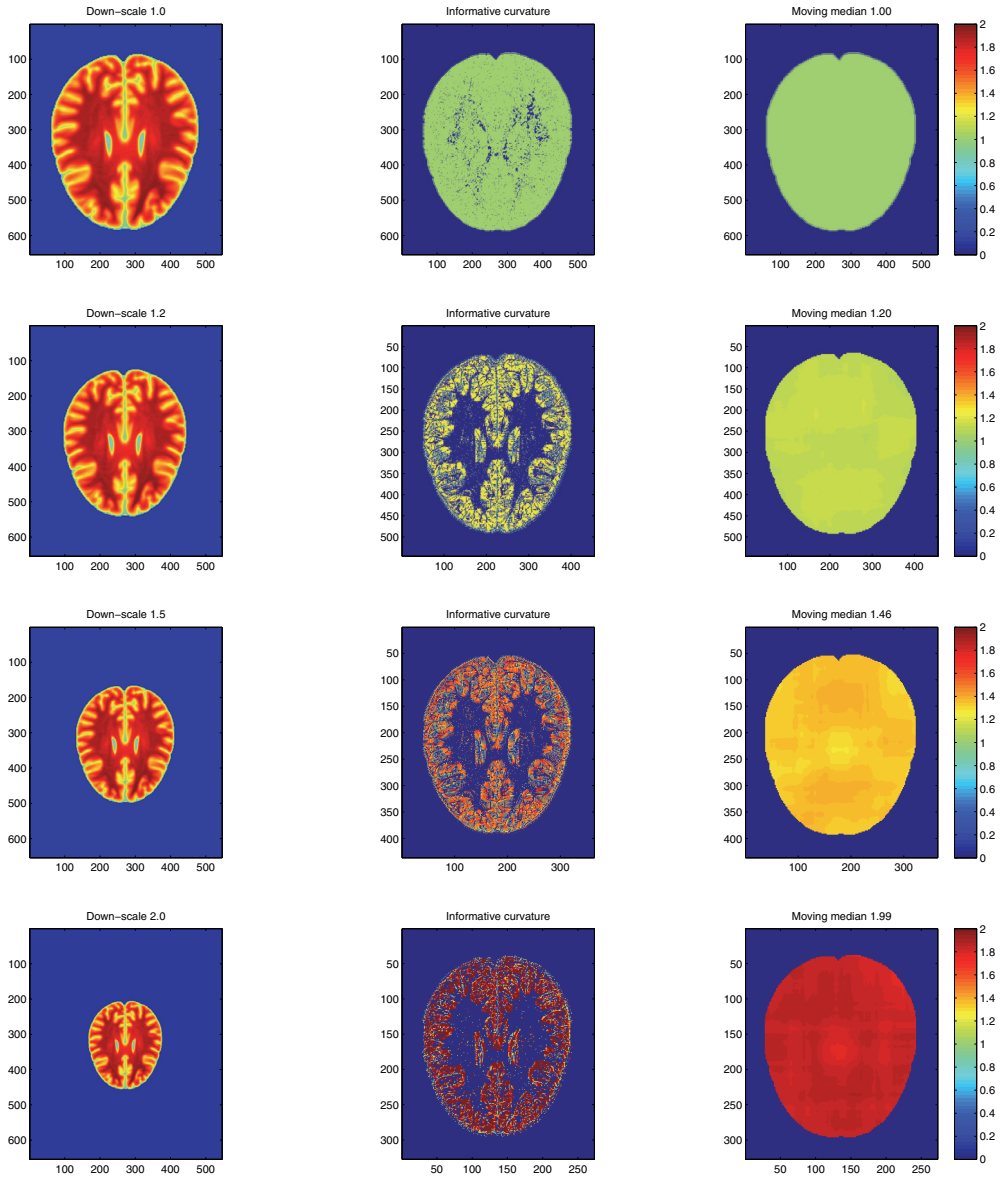

Figure 3. *A horizontal slice of an MRI scan of the brain was rescaled multiple times (left). The change in the level sets' curvature was evaluated before and after the transformation. The ratio between curvatures with nonvanishing quantities (middle) shows that many points pose enough information to evaluate scaling. Using a moving median filter, we fill up the gaps for the entire slice (right). On top of each figure we added the true scaling factor (left) and the approximated one (right).*

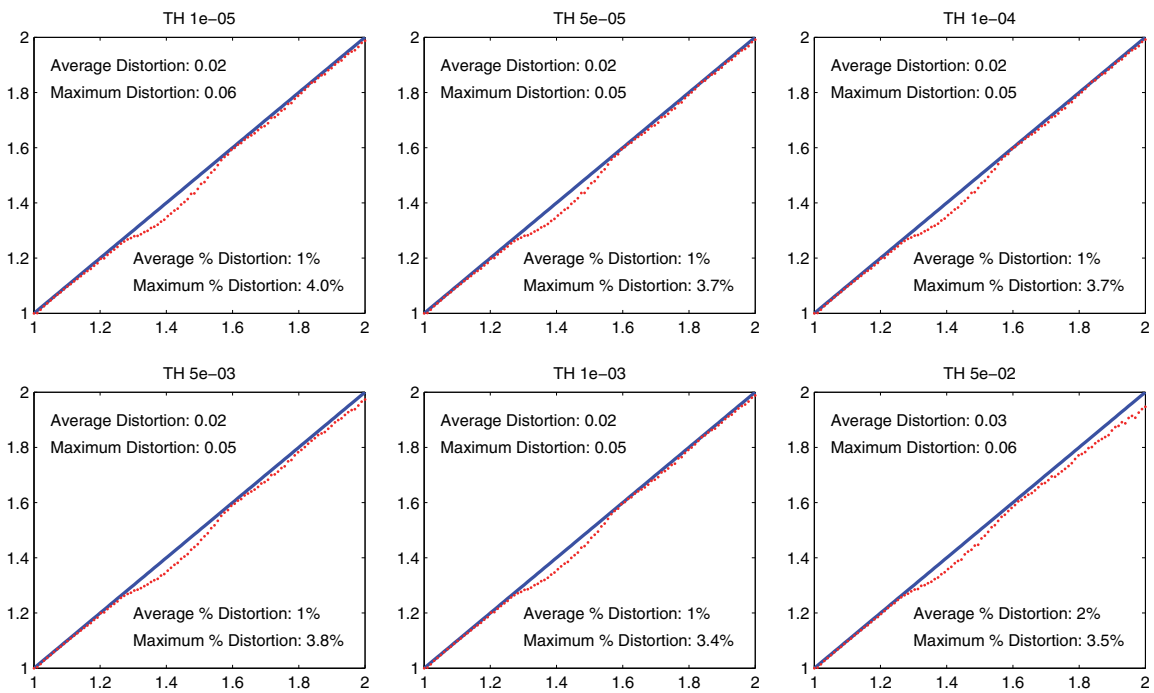

Figure 4. *A horizontal slice of an MRI scan of the brain was rescaled multiple times, and local curvature was evaluated. We explored different thresholds from* 10^{-5} *to* 5×10^{-2} *of the magnitude of the measured curvature, deciding whether a point should be considered an inlier. In each graph the* x *axis is the generated scaling, and the* y *axis is the computed one. A perfect result would have been the blue line, while the dotted curve was the calculated one. We added maximum and average distortions as absolute values and relative percentages.*

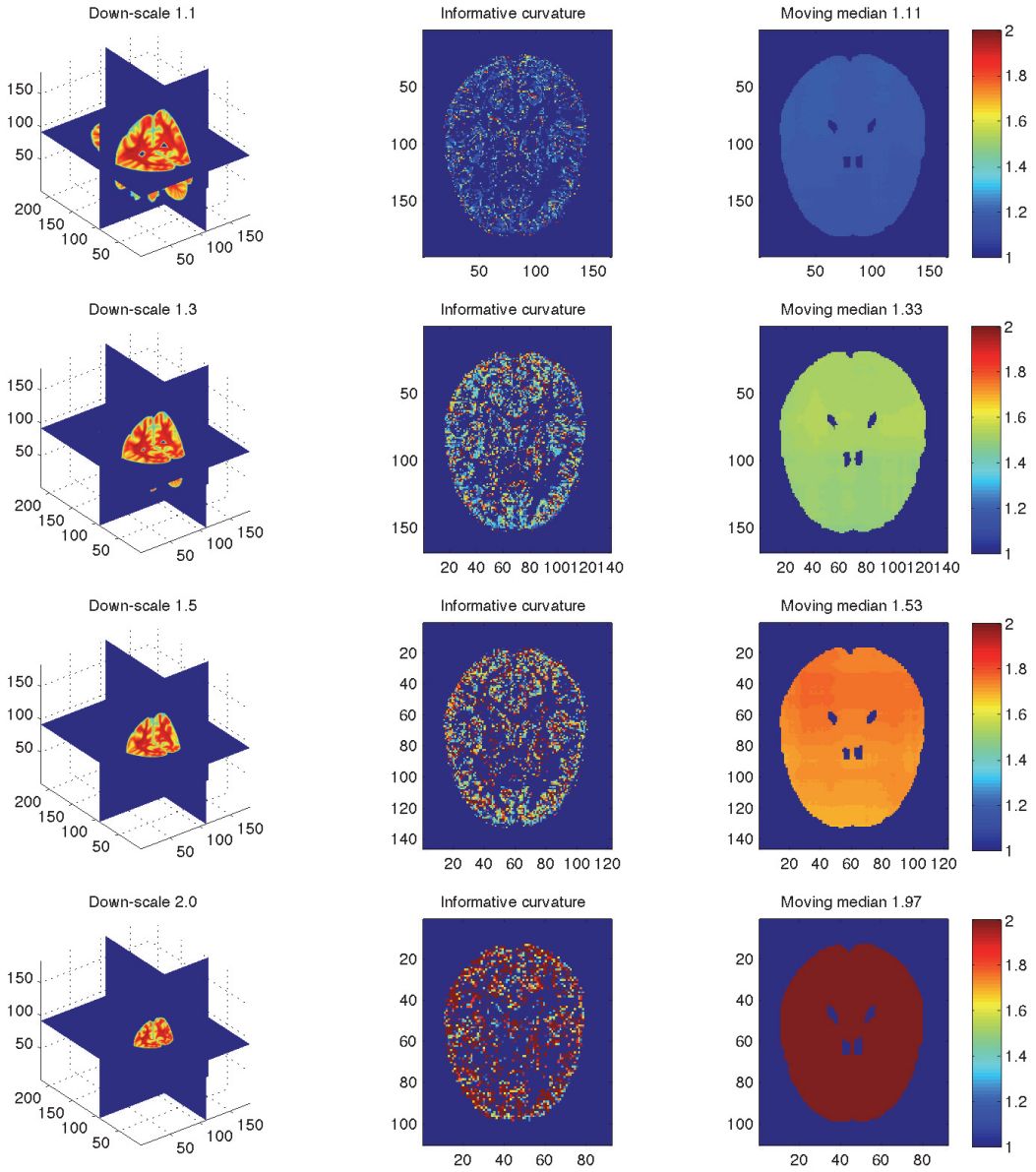

Figure 5. *An MRI (volumetric) scan of the brain was rescaled multiple times (per row). The change in the level sets' curvature was evaluated before and after the transformation. The ratio between square root of the curvatures with nonvanishing quantities (middle) shows that many points pose enough information to evaluate local scaling. Using a moving median filter, we can fill up the gaps for the entire brain (right). All the evaluations were done directly on the volume, while we depict just one slice in the second and third columns. On top of each figure we added the true scaling factor (left) and the approximated one (right).*

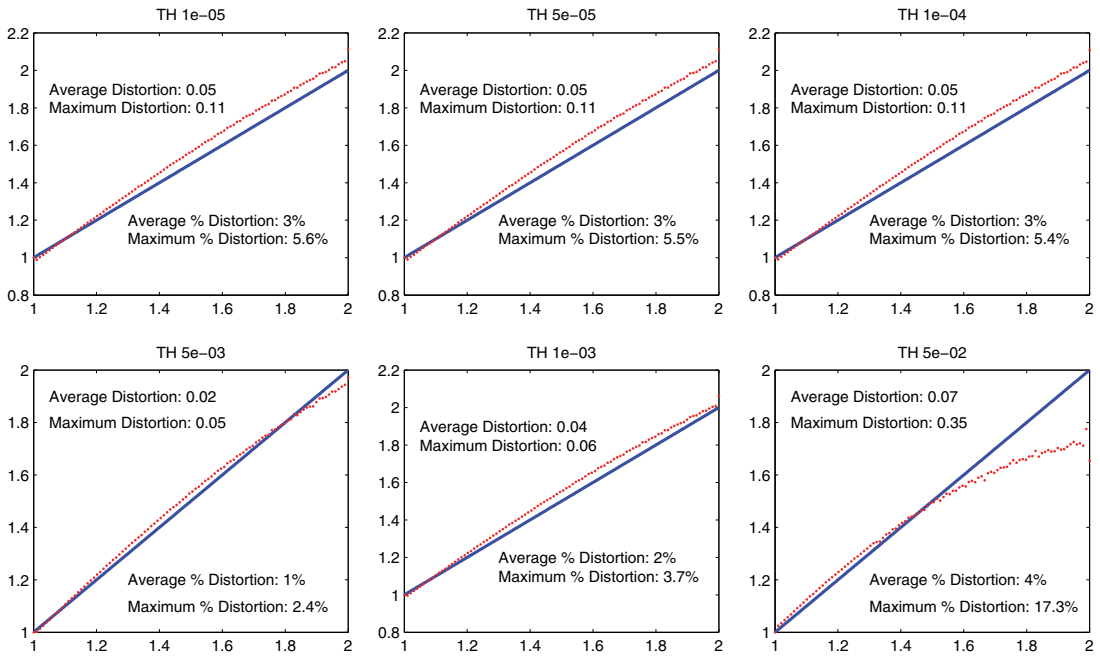

Figure 6. *A volumetric MRI scan of the brain was rescaled multiple times, and local curvature was evaluated. We explored different thresholds from* 10^{-5} *to* 5×10^{-2} *of the magnitude of the measured curvature, deciding whether a point should be considered an inlier. In each graph the* x *axis is the generated scaling, and the* y *axis is the computed one. A perfect result would have been the blue line, while the dotted curve was the calculated one. We added maximum and average distortions as absolute values and relative percentages.*

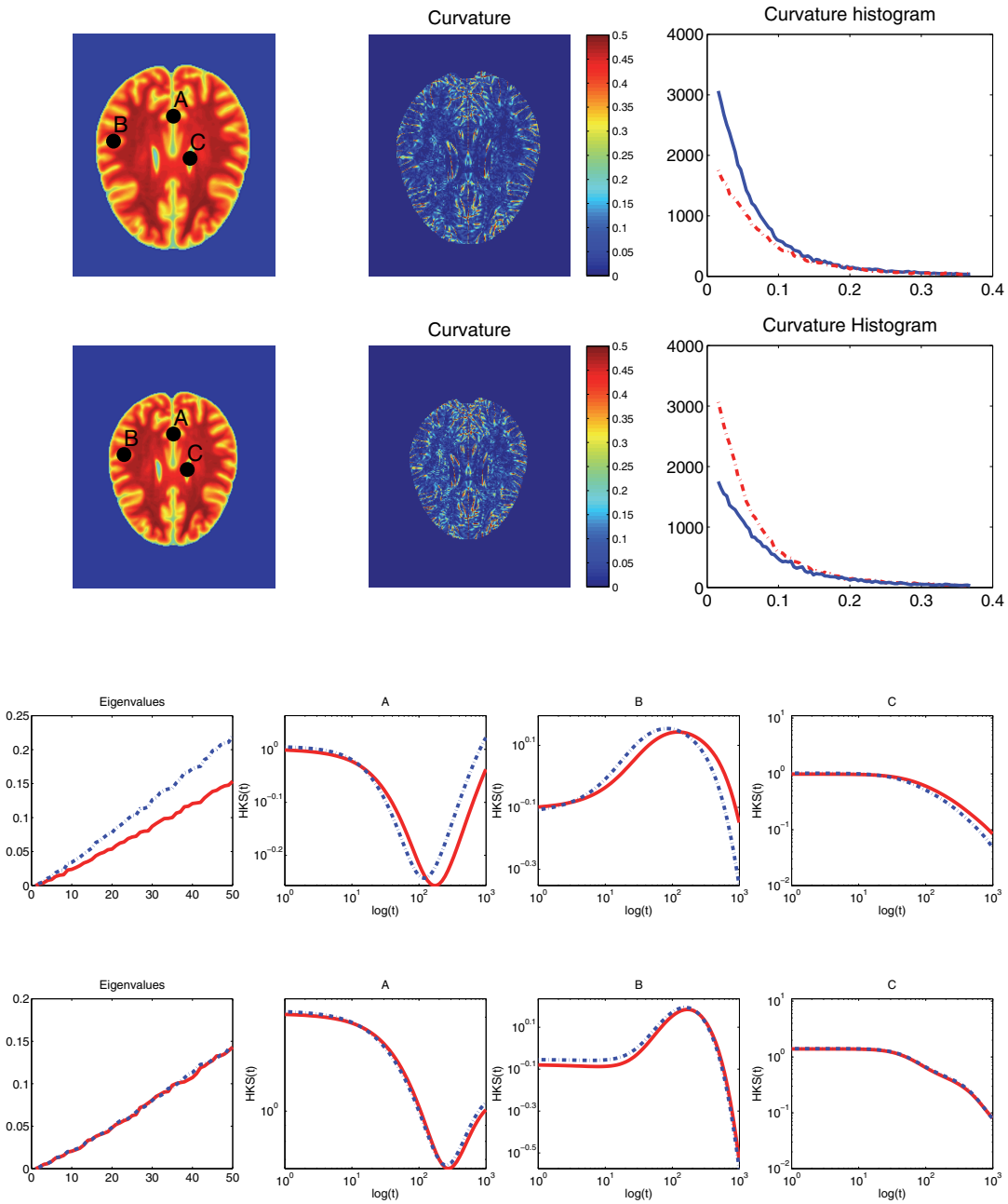

Figure 7. *Two scaled images (×1.2) with three chosen points (left, rows one and two), magnitude of level set curvature (middle column, rows one and two), and their relevant histograms (right, rows one and two). In dotted red we depict the histogram of the relevant model and in blue the histogram of the scaled (second) one. We evaluated the Laplace–Beltrami operator (rows three and four) using the Euclidean metric (third row) and the scale invariant metric (fourth row). On the left we depict the eigenvalues, and from the second column and above we show the HKS of three matching points in log-log axes.*

Finally, we evaluated commute time distances in a volumetric domain. In Figure 8 we depict the accumulating histogram of distances from the center of the brain and from a point near the cortex's boundary. The curvature used here for normalizing the volumetric structure is noisier than that measured on each slice separately, yet the results are appealing. Notice that we do witness some degradation in quality near the boundary.

We must emphasize that the experiments done in this section are influenced by the interpolation of the data as we tried to simulate the harder-case scenario of a fixed sized image rather than changing the distance between pixels.

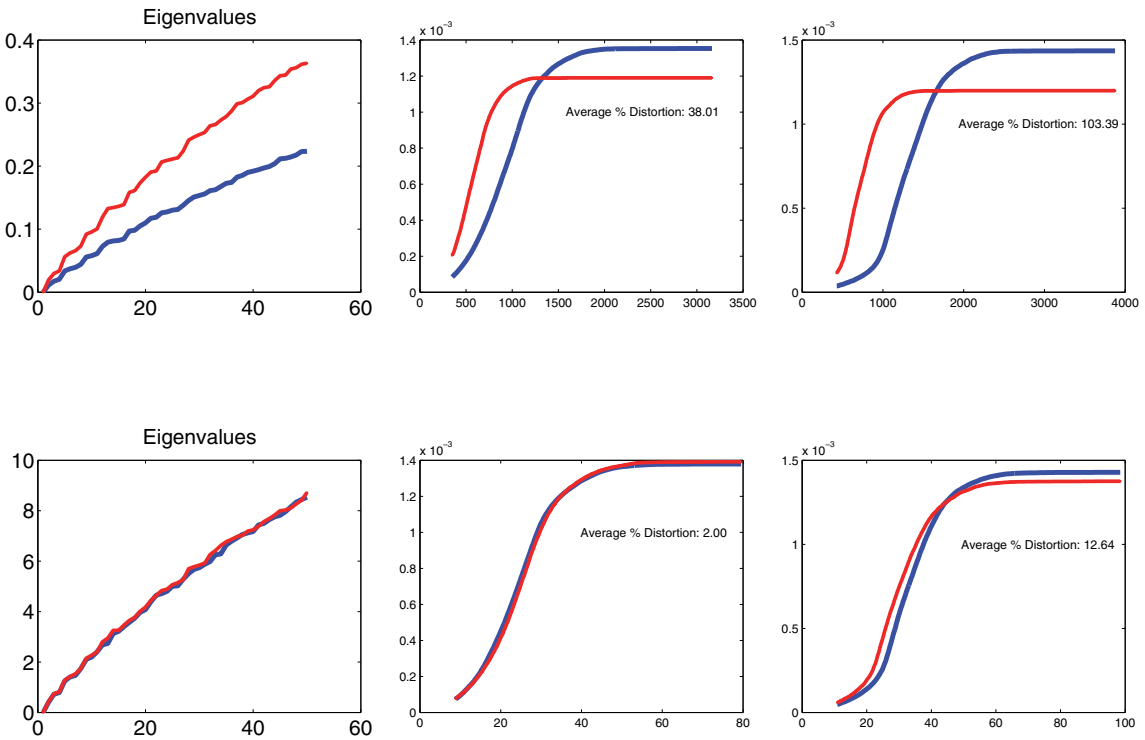

Figure 8. *Accumulated histograms of commute time distances measured from the center of the brain (middle column) and near the cortex (right column). The brain was scaled by a factor of* 1.3. *We used the Euclidean metric in the first row and the level-set scale invariant volumetric metric on the second. The first* 50 *eigenvalues are depicted in the first column.*

8. Discussion and conclusions. First order derivatives define distances and features and are the main building blocks in inference and comparison methods of shapes and structures. Second order derivatives provide additional information on curvature. This knowledge can then be used to normalize the geometry into a canonical form which is scale invariant. We recently learned how to do so for surfaces, and in this paper we further researched that using level sets and focused on volumetric datasets. We considered two different scenarios: (a) scale

invariant tensors (compensating for geometric and photometric deformations), and (b) scale invariant level sets (compensating just for geometric deformations).

Two limitations should be taken into account using differential invariants. The first is stability, as second order derivatives are more sensitive to noise and require a smooth version of the structure. This challenge was addressed by us and others, and feasible solutions exist. Here, as an example, we measured diffusion distances and HKS given the weak form of the heat equation which handles noise gracefully. The second limitation appears in locations where no curvature exists. In addition, next to such locations the curvature is unstable and requires gentle handling. We interpolated the information about the curvature using a sliding window with a median filter. Other, more robust and sophisticated, approaches exist. We chose a simple one to emphasize that this limitation can be easily addressed.

9. Summary. We presented two scale invariant metrics for volumetric data. One compensates for the change in geometry and photometry, while the second focuses on the geometric part alone. We provided theoretical results and showed different examples on an MR atlas. Generating scale-free features is the first step toward improving alignments and inference of geometric datasets. Here we introduced one important building block for such tasks.

REFERENCES

[1] Y. Aflalo, R. Kimmel, and D. Raviv, *Scale invariant geometry for nonrigid shapes*, SIAM J. Imaging Sci., 6 (2013), pp. 1579–1597.

[2] H. Bay, T. Tuytelaars, and L. Van Gool, *SURF: Speeded up robust features*, in Computer Vision–ECCV 2006, Lecture Notes in Comput. Sci. 3951, Springer, Berlin, 2006, pp. 404–417.

[3] P. Bérard, G. Besson, and S. Gallot, *Embedding Riemannian manifolds by their heat kernel*, Geom. Funct. Anal., 4 (1994), pp. 373–398.

[4] A. M. Bronstein, M. M. Bronstein, and R. Kimmel, *Three-Dimensional Face Recognition*, US Patent Application 20040076313 A1, 2004.

[5] A. M. Bronstein, M. M. Bronstein, and R. Kimmel, *Expression-invariant face recognition via spherical embedding*, in International Conference on Image Processing (ICIP), Vol. 3, IEEE, Washington, DC, 2005, pp. 756–759.

[6] A. M. Bronstein, M. M. Bronstein, and R. Kimmel, *Generalized multidimensional scaling: A framework for isometry-invariant partial surface matching*, Proc. Natl. Acad. Sci. USA, 103 (2006), pp. 1168–1172.

[7] A. M. Bronstein, M. M. Bronstein, R. Kimmel, M. Mahmoudi, and G. Sapiro, *A Gromov-Hausdorff framework with diffusion geometry for topologically-robust non-rigid shape matching*, Internat. J. Comput. Vision, 89 (2010), pp. 266–286.

[8] A. M. Bruckstein, R. J. Holt, A. N. Netravali, and T. J. Richardson, *Invariant signatures for planar shape recognition under partial occlusion*, Comput. Vision Image Understanding, 58 (1993), pp. 49–65.

[9] A. M. Bruckstein, N. Katzir, M. Lindenbaum, and M. Porat, *Similarity-invariant signatures for partially occluded planar shapes*, Internat. J. Comput. Vision, 7 (1992), pp. 271–285.

[10] A. M. Bruckstein, E. Rivlin, and I. Weiss, *Scale space semi-local invariants*, Image Vision Comput., 15 (1997), pp. 335–344.

[11] T. Cohignac, C. Lopez, and J. M. Morel, *Integral and local affine invariant parameter and spplication to shape recognition*, in Proceedings of the 12th IAPR International Conference on Pattern Recognition, Vol. 1, IEEE, Washington, DC, 1994, pp. 164–168.

[12] R. R. Coifman and S. Lafon, *Diffusion maps*, Appl. Comput. Harmon. Anal., 21 (2006), pp. 5–30.

[13] R. R. Coifman, S. Lafon, A. B. Lee, M. Maggioni, B. Nadler, F. Warner, and S. W. Zucker, *Geometric diffusions as a tool for harmonic analysis and structure definition of data: Diffusion maps*, Proc. Natl. Acad. Sci. USA, 102 (2005), pp. 7426–7431.
[14] M. P. DoCarmo, *Riemannian Geometry*, Birkhäuser Boston, Boston, MA, 1992.
[15] A. Elad, Y. Keller, and R. Kimmel, *Texture mapping via spherical multi-dimensional scaling*, in Proceedings of Scale-Space Theory in Computer Vision, 2005, pp. 443–455.
[16] A. Elad and R. Kimmel, *Bending invariant representations for surfaces*, in Proceedings of the IEEE Computer Society Conference on Computer Vision and Pattern Recognition (CVPR), IEEE, Washington, DC, 2001, pp. 168–174.
[17] R. Goldman, *Curvature formulas for implicit curves and surfaces*, Comput. Aided Geom. Design, 22 (2005), pp. 632–658.
[18] A. B. Hamza and H. Krim, *Geodesic matching of triangulated surfaces*, IEEE Trans. Image Process., 15 (2006), pp. 2249–2258.
[19] R. Kimmel and J. A. Sethian, *Computing geodesic paths on manifolds*, Proc. Natl. Acad. Sci. USA, 95 (1998), pp. 8431–8435.
[20] R. Kimmel, N. Sochen, and R. Malladi, *From high energy physics to low level vision*, in Scale-Space Theory in Computer Vision, Lecture Notes in Comput. Sci. 1252, Springer, Berlin, 1997, pp. 236–247.
[21] A. Kovnatsky, M. M. Bronstein, D. Raviv, A. M. Bronstein, and R. Kimmel, *Affine-invariant photometric heat kernel signatures*, in Proceedings of the 5th Eurographics Conference on 3D Object Retrieval (3DOR), Eurographics Association, Aire-la-Ville, Switzerland, 2012, pp. 39–46.
[22] Y. Lipman and T. Funkhouser, *Möbius voting for surface correspondence*, in Proceedings of SIGGRAPH, ACM Trans. Graphics 28, ACM, New York, 2009.
[23] D. Lowe, *Distinctive image features from scale-invariant keypoint*, Internat. J. Comput. Vision, 60 (2004), pp. 91–110.
[24] T. Moons, E. J. Pauwels, L. J. Van Gool, and A. Oosterlinck, *Foundations of semi-differential invariants*, Internat. J. Comput. Vision, 14 (1995), pp. 25–48.
[25] J. M. Morel and G. Yu, *ASIFT: A new framework for fully affine invariant image comparison*, SIAM J. Imaging Sci., 2 (2009), pp. 438–469.
[26] M. Ovsjanikov, A. M. Bronstein, M. M. Bronstein, and L. J. Guibas, *Shape Google: A computer vision approach to invariant shape retrieval*, in Proceedings of the 2nd Workshop on Non-Rigid Shape Analysis and Deformable Image Alignment (NORDIA), Kyoto, Japan, 2009, pp. 1–20.
[27] M. Ovsjanikov, Q. Mérigot, F. Mémoli, and L. J. Guibas, *One point isometric matching with the heat kernel*, Computer Graphics Forum, 29 (2010), pp. 1555–1564.
[28] E. J. Pauwels, T. Moons, L. J. Van Gool, P. Kempenaers, and A. Oosterlinck, *Recognition of planar shapes under affine distortion*, Internat. J. Comput. Vision, 14 (1995), pp. 49–65.
[29] H. Qiu and E. R. Hancock, *Commute Times, discrete Green's functions and graph matching*, in Proceedings of the International Conference on Image Analysis and Processing (ICIAP), Cagliari, Italy, 2005, pp. 454–462.
[30] D. Raviv, A. M. Bronstein, M. M. Bronstein, D. Waisman, N. Sochen, and R. Kimmel, *Equi-affine invariant geometry for shape analysis*, J. Math. Imaging Vision, 50 (2014), pp. 144–163.
[31] D. Raviv and R. Kimmel, *Affine invariant geometry for non-rigid shapes*, Internat. J. Comput. Vision, 111 (2015), pp. 1–11.
[32] D. Raviv, J. Lessick, and R. Raskar, *Evaluating local contractions from large deformations using affine invariant spectral geometry*, in Proceedings of the International Workshop on Statistical Atlases and Computational Modeling of the Heart, Boston, MA, 2014, pp. 147–157.
[33] G. Sapiro, *Affine Invariant Shape Evolutions*, Ph.D. thesis, Technion - Israel Institute of Technology, Haifa, Israel, 1993.
[34] S. M. Smith, M. Jenkinson, M. W. Woolrich, C. F. Beckmann, T. E. J. Behrens, H. Johansen-Berg, P. R. Bannister, M. De Luca, I. Drobnjak, D. E. Flitney, R. Niazy, J. Saunders, J. Vickers, Y. Zhang, N. De Stefano, J. M. Brady, and P. M. Matthews, *Advances in functional and structural MR image analysis and implementation as FSL*, Neuroimage, 23 (2004), pp. 208–219.
[35] M. Spivak, *A Comprehensive Introduction to Differential Geometry*, Brandeis University, Waltham, MA, 1970.

[36] J. Sun, M. Ovsjanikov, and L. J. Guibas, *A concise and provably informative multi-scale signature based on heat diffusion*, in Proceedings of the Symposium on Geometry Processing (SGP), Berlin, Germany, 2009, pp. 1383–1392.

[37] Y. Wang, M. Gupta, S. Zhang, S. Wang, X. Gu, D. Samaras, and P. Huang, *High resolution tracking of non-rigid motion of densely sampled 3D data using harmonic maps*, Internat. J. Comput. Vision, 76 (2008), pp. 283–300.

[38] L. Yatziv, A. Bartesaghi, and G. Sapiro, *O(N) implementation of the fast marching algorithm*, J. Comput. Phys., 212 (2006), pp. 393–399.